Performance assessment of industrial-sized solid oxide cells operated in a reversible mode: Detailed numerical and experimental study

Vanja Subotić [a],*, Thomas Thaller [a], Benjamin Königshofer [a], Norbert H. Menzler [b], Edith Bucher [c], Andreas Egger [c], Christoph Hochenauer [a]

[a] Institute of Thermal Engineering, Graz University of Technology, Inffeldgasse 25/B, 8010, Graz, Austria
[b] Forschungzentrum Jülich GmbH, Institute of Energy and Climate Research (IEK), IEK-1: Materials Synthesis and Processing, 52425 Jülich, Germany
[c] Chair of Physical Chemistry, Montanuniversitaet Leoben, Franz-Josef-Straße 18, 8700, Leoben, Austria

HIGHLIGHTS

- Time-efficient spatially-resolved model for industrial-sized rSOCs.
- Detailed performance assessment based on numerical and experimental study.
- Model validation based on in-house made cells and experiments.
- Very good accordance between measured and simulated EIS, DRT and U/i data.
- Comparison of co-flow and counter-flow conditions for rSOC operation.

ARTICLE INFO

ABSTRACT

Reversible solid oxide cells (rSOCs) present a unique possibility in comparison to other available technologies to generate electricity, heat and valuable fuels in one system, in a highly-efficient manner. The major issue hindering their commercialization are system reliability and durability. A detailed understanding of the processes and mechanisms that occur within rSOCs of industrial-size, is of critical importance for addressing this challenge. This study provides in-depth insight into behavior of large planar rSOCs based on a comprehensive experimental and numerical study. All the numerical data obtained are validated with the in-house made cells and experiments. The sensitivity analysis, which covers a wide range of operating conditions relevant for industrial-sized systems, such as varying operating temperature, H_2/H_2O-ratio, operating current etc., provides very good accordance of the cell performance measured and simulated. It reveals that lowering fuel volume and thus causing fuel starvation has more pronounced effect in an electrolysis mode, which is visible in both the low-frequency and the middle-frequency range. Moreover, both co- and counter-flow are appropriate for the reversible operation. However, more uniform current density distribution is achievable for the counter-flow, which is of crucial importance for the real system design. The most accurate performance prediction can be achieved when dividing the cell into 15 segments. Slightly lower accuracy is reached by logarithmic averaging the fuel compositions, thus reducing the calculation time

* Corresponding author.
    E-mail address: vanja.subotic@tugraz.at (V. Subotić).

required. A computationally- and time-efficient model with very precise performance prediction for industrial-sized cells is thus developed and validated.

Introduction

An increased share of renewable energies in the European electricity production mix brings additional uncertainties regarding planning and prediction of available capacity. In order to still be able to provide security of supply and grid stability a higher flexibility of energy supply systems is necessary. This can be achieved by expansion of energy storage systems, which store energy during phases of excess availability and then feed back into the grid according to demand [1–3]. Reversible solid oxide cells (rSOC), which are able to generate both electricity and heat in fuel cell mode and to produce valuable fuels in electrolysis mode are considered to be a promising technology for hydrogen-based energy storage systems [4]. It has to be noted here that rSOC systems are to date the only available technology, which can operate in fuel cell and electrolysis mode in one single system. Any other technology needs at least two separate systems.

One major challenge of rSOCs is the degradation of cell performance over time. Recent advances in materials engineering and processing technologies extended fuel cell lifetime and significantly reduced degradation rates down to 0.5%/1000 h, even for extremely long operation times (> 10,000 h) [5–7]. Nevertheless, cells optimized for fuel cell mode present significantly higher degradation rates of 2–5%/1000 h when operated in electrolysis mode [8,9]. While the most frequent degradation modes occurring on the hydrogen electrode are caused by contaminants or impurities in fuel cell mode or as a consequence of Ni-spreading and Ni-loss in electrolysis mode [10,11], the performance of the oxygen electrode is mainly affected by delamination of the interface oxygen electrode/electrolyte layer and the formation of secondary phases [5]. Degradation of the electrolyte can occur as a consequence of formation of defect associates, which reduce the mobility of oxygen vacancies in the crystal lattice and microcracks [12] or prevented diffusion processes, formation of Kirkendall voids [13,14] and the formation of oxygen in the electrolyte [15]. Nevertheless, besides the material issues, which cause long-term degradation, specific operating conditions can lead to the accelerated degradation. In order to enable a reliable operation and longevity of reversible solid oxide cells, the design of experiments has to be carefully planned. This includes taking into account operating parameters such as current density, voltage, temperature and gas composition. Therefore, in order to select suitable operational conditions to reduce degradation rates, it is essential to gain detailed understanding of reactions and processes that occur in rSOC cells, their impact on the cell performance and subsequent possible degradation mechanisms [5,16,17].

Individual processes and process parameters in the rSOC system are difficult to access experimentally, but can be easily accessible when using simulation tools. Depending on the application of a model developed and the requirements in terms of accuracy and scale, different model approaches have been developed. In black box models the transmission behavior is determined between predefined input and output parameters which are based on existing data, whereby the system structure and physical backgrounds are not taken into account [18,19]. More complex gray box models utilize the basic structure of the system, while the single elements are also parameterized by measured data. The modeling of the cell behavior based on physical laws is an alternative approach, which enables the identification of processes and their connection to chemical, physical and geometrical properties [20,21]. 0D thermodynamic models represent a simple solution for simulation of the performance achievable, e.g. reactions within electrolysers and fuel cells are considered simply as catalytic reactions [22]. While 1D physical electrochemical models provide detailed information on mass transport, heterogeneous chemistry and porous media transport, they also require a strong dependency the output parameters on the input parameters such as operating conditions [23]. 1D models are presented to be able to analyse a dynamic behavior of both SOFC and SOEC and to suggest appropriate control strategies [24,25]. Advanced 2D models offer deeper insight into the spatially-resolved rSOC performance such as local temperature, current and potential distribution, gas distribution, heat fluxes and overpotentials while also giving information about their impact on the overall performance [26,27]. In Ref. [28] a 2D-transient single channel model is developed to illustrate performance of rSOC when operating under hydrogen and syngas. Detailed simulations led to the conclusion that an H_2/H_2O mixture is more appropriate for a reversible operation, while the operation under syngas can be seen as challenging in terms of switching between the two operating modes. State-of-the-art 3D models with commercial computational fluid dynamics codes provide very precise information on species distribution of the chemical and electrochemical reactions [29]. 3D simulations can also be used in a very effectively manner to improve performance of SOC or even for making a selection of the most appropriate material designs to enhance electrochemical reactions. In Ref. [30] the authors developed a novel porous flow-field design based on a 3D-model and compared it with several other material designs, thus enabling an optimization of the SOEC system. Moreover, when expanding the model from the single-cell up to the stack level, very important information relating to both operation stability and system durability can be obtained. Knowledge about the transient thermal behavior

of cells and stacks is of great importance in order to predict mechanisms that can trigger thermomechanical degradation mechanisms and thus for designing the operating environment with the aim of ensuring a stable degradation-free stack operation, as shown in Ref. [31]. Next, on the system level, the energy analysis for a 10 kW power to gas system performed in Ref. [32] showed possibilities for increasing the efficiency of the electrolysis systems. However, according to the authors' best knowledge, there is still no model available for industrial-sized rSOCs, which enables very detailed performance simulation considering various operating conditions relevant for real application, and that is validated by in-house made cells and experiments.

Scope of this study

This work focuses on the numerical and experimental investigations of industrial-sized solid oxide cells operated in a reversible mode. A detailed physical model based on 120 equations was built to analyse cell performance in both operating modes and to obtain a detailed insight into processes and loss mechanisms. By carefully selecting the fundamental equations, quantitative predictions for operation in both fuel cell and electrolysis mode can be made, ensuring extensive validation of the model and detailed investigation of loss mechanisms.

All the data simulated are validated by experimental results acquired for the purpose of this study. A mixture of hydrogen, water vapor and nitrogen was employed as fuel. A very good accordance between the simulated and measured data was achieved and the results observed enabled: (i) better understanding of single processes, which is not possible with purely experimental investigations, (ii) making suggestions for the improvement of the experimental setup, and (iii) very detailed presentation of performance achievable for industrial-sized rSOCs. It is important to mention here that the aim of the experimental study was not to achieve the maximum performance of the cells employed. The cells were embedded in a housing and the setup was prepared to have slight leakages and not ideal contacting of the electrodes and contacting meshes. This makes it possible to simulate such failure modes and to see their impact in the simulation results, when simulating systems of industrial scale, and also for determining failures of this kind when operating the cells and systems. A physical model of a planar rSOC developed enables the predicting of polarization curves, electrochemical impedance performance and distribution of relaxation times under different operating conditions, thus including varying operating temperatures, fuel and air volume flows, fuel and air/oxygen composition, as well as flow conditions. One of the most common methods for analysis of processes in fuel cells, the electrochemical impedance spectroscopy (EIS), was applied in-operando as a state of health diagnosis method. The data obtained were used to derive and interpret the equivalent circuit model (ECM) and evaluate distribution of relaxation times (DRT), or simply to analyse geometrical aspects of the EIS curve. ECM is a combination of ideal electrical elements that simulate charge transfer, mass transport and other processes. DRT is sort of an equivalent way to express

information contained in ECM, in which the frequency-dependent impedance values are converted into a spectrum of serially connected RC-elements according to their relaxation times [21,33–35]. This makes it easier to differentiate between the individual loss mechanisms, even if the associated time constants are close together. The measured and simulated results could thus be compared with each other.

Although the model enables very detailed analysis of rSOCs in both operating modes, the aim was not to develop complex 3D models, which are computationally- and time-intensive, but the model, which gives as much detailed information as possible in a time-efficient manner. The model presented in this study was developed in MATLAB and according to the authors' best knowledge no such model is currently present in the literature. It is based on the physical laws and presents a time-efficient solution for very detailed performance assessment of industrial-sized rSOCs, which is of crucial importance for development, operation and optimization of rSOC systems. For its validation in-house made cells and experimental data are used. The model developed can easily be implemented into available tools for prediction of cell performance, comparison of monitored and predicted performances and thus also be used to extend control algorithms.

Experimental setup

The experimental investigations were carried out on single-cells embedded in a ceramic-cell housing and the data obtained were used to validate the model developed. For this purpose, voltage monitoring, polarization curve, electrochemical impedance spectroscopy (EIS), extensive temperature measurements and off-gases analysis were conducted. Fuel electrode-supported solid oxide cells (further in the text referred as SOC) were employed. The fuel electrode was fabricated as Ni/YSZ, mixing raw nickel oxide powder with 8 mol% YSZ and sintering it at approximately 1,200 °C for 5 h. Afterwards, the anode composed of NiO and 8YSZ was screen-printed on the YSZ support. In order to ensure the gas-tightness of the 8YSZ electrolyte, it was co-fired at 1,400 °C for 5 h. A barrier layer between the electrolyte and the cathode was composed of GDC. On the top of it, the LSCF perovskite cathode was screen-printed and sintered at 1,080 °C. The overall area of the single-cells was 10 cm × 10 cm with an active area of 80 cm^2. The cell geometry is illustrated in Fig. 3b.

An illustration of the test rig used is provided in Fig. 1. The cells were embedded in a ceramic cell housing, which was fabricated as alumina. When using a ceramic cell housing it is possible to avoid unwanted failure, which could occur when employing metallic cell housing. The cell anode and cathode were supplied with gas via gas pipes. The gas inlet and outlet pipes are ceramic and heated up to the operating temperature in an electrical furnace. The operating temperature was varied between 700 °C, 750 °C and 800 °C for the purpose of the detailed investigations. The fuel electrode was supplied with a mixture of hydrogen/steam/nitrogen, since the cells are operated in a reversible mode. The same gas composition can thus be used in both operating modes.
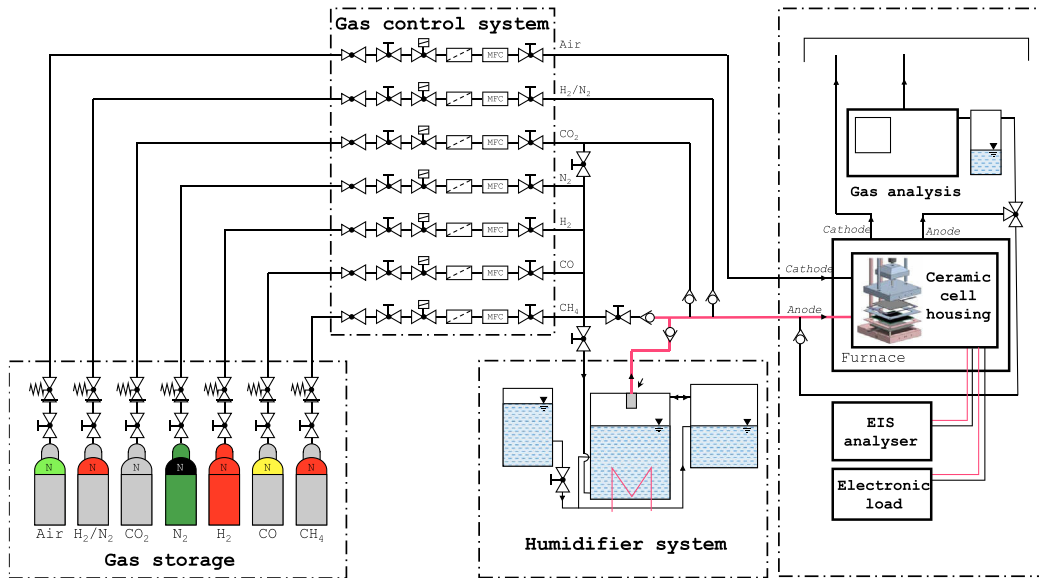
Fig. 1 — Comparison of cell performance when varying operating temperature, fuel volume flow and oxygen concentration on the oxygen electrode.

Hydrogen is always required at the fuel electrode inlet in order to prevent oxidation of the anode in a fuel cell mode and cathode in an electrolysis mode, respectively. In parallel, the air electrode is supplied with air. The operating parameters applied for experimental investigations, thus considering gas composition, fuel and air volume flow and operating temperature, are shown in Table 1. Volume flow of individual gas components was controlled using mass flow controllers (MFC). An ABB gas analyser is used for analyzing the volumetric fraction of single gas components at both the anode inlet and outlet sides.

In order to achieve a desired degree of gas-tightness between the electrodes, glass sealing was used. In addition, ceramic frames were used. Ni-meshes were used for contacting on the fuel electrode. A platinum mesh was applied on the oxygen electrode. The temperature was measured at 6 different points on the fuel electrode, 6 points on the oxygen electrode as well as on the fuel and air inlet and outlet (4 points). A mechanical load was applied, which can be increased up to 1 kg/cm^2, in order to decrease the contacting resistance. A more detailed description of the cell housing can be found elsewhere [36–38].
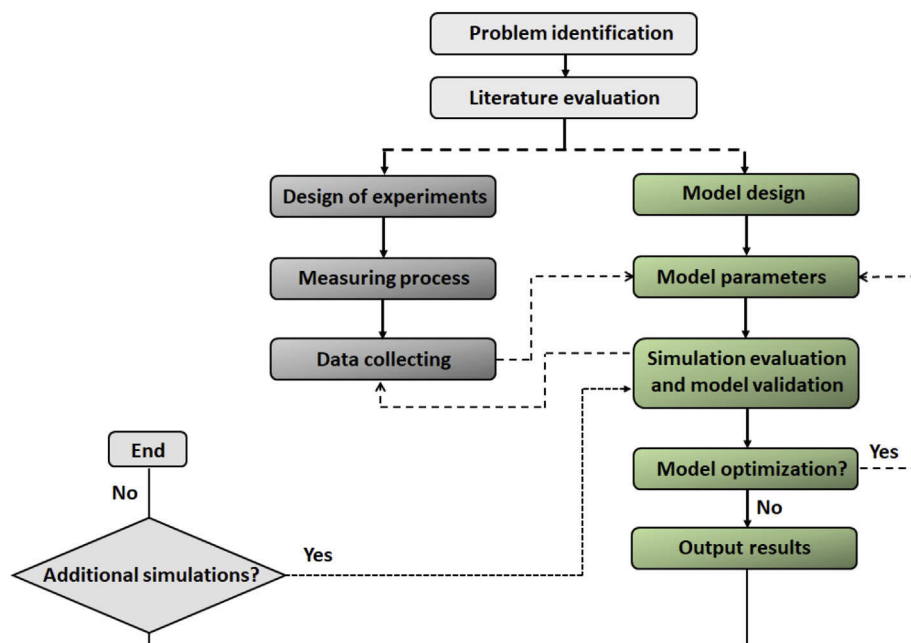

Fig. 2 — Flow chart showing the basic principle of modeling and experiments.

(a) Scheme of a channel cross-section.

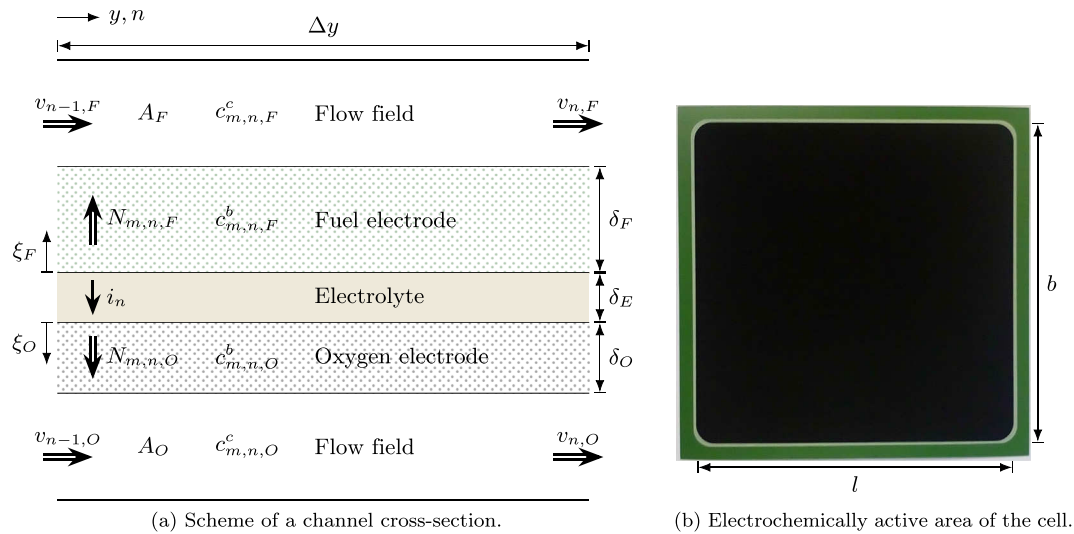(b) Electrochemically active area of the cell.

Fig. 3 – Basic overview of a simulation model.

For the purpose of electrochemical analysis, measurements of polarization curves and electrochemical impedance spectroscopy were performed. A Bio-Logic impedance analyser with an 80-A booster was employed for this purpose. It is designed for 4-quadrant operation and can thus be used both as a potentionstat and a galvanostat, with an option to control DC and AC signals. Before starting electrochemical measurements, an effort was made to achieve a state of equilibrium. The polarization curve measurements were performed by applying the current ramp of 40 mA/s. The impedance measurements were performed in a galvanostatic mode, by superimposing an AC current wave in the frequency range 100 mHz-10 kHz with 10 points/decade. Since the booster was used, the maximum frequency was limited to 10 kHz. The AC value was set to a count of 4% of the DC value for the specific operating point. The EIS measurements were performed in the entire load range. The impedance data obtained were further analyzed by applying distribution of relaxation times methodology and the software used for this is detailed explained in Ref. [34].

Creation of a simple model for rSOC simulation

In order to both numerically examine and predict performance of the reversibly operated SOCs of industrial size, a model based on physical parameters was built. The equations used are selected to be appropriate for both the fuel cell and the electrolysis mode. Employing the fundamental model equations it is possible to simulate polarization curves, electrochemical impedance spectroscopy and detailed loss distributions. A total of 120 equations were employed for the model development. They enable to integrate thermodynamics, charge transfer, mass transfer in both electrodes and flow field, and reaction kinetics into an advanced model. The boundary conditions are set based on the experimental setup, described in the previous section. A detailed explanation of all the parameters used in the equations can be found in the list of symbols. We will not show all of the equations that were used in this study, but only the most representative ones. In this section, the detailed insight into the modeling steps is

Influencing variable	ϑ	Fuel electrode				Oxygen electrode		
		x_{H_2}	x_{H_2O}	x_{N_2}	$\dot{V}_F$	x_{O_2}	x_{N_2}	$\dot{V}_O$
Variants (Abbreviation)	°C	%	%	%	SLPM	%	%	SLPM
Temperature								
(T)	700	30	30	40	2	21	79	1.6
	750	30	30	40	2	21	79	1.6
	800	30	30	40	2	21	79	1.6
Volume flow								
Fuel electrode (V)	750	30	30	40	2	21	79	1.6
	750	30	30	40	0.85	21	79	1.6
Gas composition - Fuel electrode								
(XF1)	700	45	15	40	2	21	79	1.6
(XF2)	700	30	30	40	2	21	79	1.6
(XF3)	700	15	15	70	2	21	79	1.6
Flow configuration								
Co-/Counter-flow (F)	750	30	30	40	2	21	79	1.6

Table 1 – Operating parameters used.

given, especially with regard to charge transfer, mass transfer in electrodes, mass transfer in flow field as also polarization and the impedance model.

The simplified flow chart used for carrying out experimental and numerical investigations within this study is shown in Fig. 2.

Fundamental equations

The energy conversion in fuel cells can be described focusing on the basic thermodynamic principles. The chemical reactions of crucial importance in this study are hydrogen oxidation in the fuel cell mode, and in the opposite direction, steam dissociation in the electrolysis mode:

$$H_2 + \frac{1}{2} O_2 \rightleftharpoons H_2O \tag{1}$$

Besides the macroscopic thermodynamic consideration, for which only the initial and end conditions are taken into consideration, additional information on the occurring processes can be gained by considering the reaction kinetics. In the equilibrium state, the forward and reverse reaction rates are equal and the current density that occurs is indicated as an exchange current density. Nevertheless, if the operating state diverges from the equilibrium state, the exchange current density is not equal for the forward and reverse reactions, thus resulting in the net current density, as follows [39]:

$$i = \Delta i_i = i_0^0 \cdot \left(\prod_E \left(\frac{c_m}{c^0}\right)^{|\nu_{st,m}|} \cdot e^{\alpha \cdot \frac{z_e \cdot F \cdot \eta}{R \cdot T}} - \prod_P \left(\frac{c_m}{c^0}\right)^{|\nu_{st,m}|} \cdot e^{-(1-\alpha) \cdot \frac{z_e \cdot F \cdot \eta}{R \cdot T}} \right) \tag{2}$$

in which α is the transfer coefficient, η indicates the overvoltage losses, and c is related to the species concentration.

In contrast to the ideal operating conditions, different effects occur under real operating conditions, which reduce the fuel cell performance. The deviation from the ideal voltage is specified by overvoltage losses. They can be divided into the equilibrium share (η_0), for which operating current equals zero, and the current-depending share (η_i), as follows [40]:

$$\eta = \eta_0 + \eta_i \tag{3}$$

In the equilibrium state, the current density is considered to be zero, thus leading to the following overvoltage:

$$\eta_0 = \frac{R \cdot T}{z_e \cdot F} \cdot \ln \left(\prod_{E+P} \left(\frac{c_m}{c^0}\right)^{\nu_{st,m}} \right) \tag{4}$$

Considering such overvoltage differentiation, the net current can be presented as the Butler-Volmer-Equation [35]:

$$i = i_0 \cdot \left(e^{\alpha \cdot \frac{z_e \cdot F \cdot \eta_{act}}{R \cdot T}} - e^{-(1-\alpha) \cdot \frac{z_e \cdot F \cdot \eta_{act}}{R \cdot T}} \right) \tag{5}$$

with the activation overvoltage η_{act} and the exchange current density i_0.

Moreover, the losses are divided into concentration losses, activation losses and ohmic losses. Depending on the concentration of reactants and products on the electrochemically active reaction sites in comparison to their concentration under open circuit voltage (OCV) conditions, the local

potential and thus the occurring losses vary in accordance with Eq. (6) [40].

$$\eta_{conc} = \frac{R \cdot T}{z_e \cdot F} \cdot \ln \left(\prod_m \left(\frac{c_m^*}{c_{m,0}}\right)^{\nu_{st,m}} \right) \tag{6}$$

$c_{m,0}$ refers to the concentration of the specific gaseous species at OCV and c_m^* to the local concentrations. In the present study, all the losses are related to the H_2, H_2O and O_2 components, thus differing between losses that occur on the fuel electrode and those on the oxygen electrode. Taking the electrochemical reactions that occur into account, the forward and reverse reactions are dependent on the required activation energy and thus the available potential difference, which is presented as a function of charge transfer. A deviation from the equilibrium state is thus necessary in order to initiate the occurrence of reactions, and thus simultaneously leading to the irreversible entropy increases and losses [41]. For a special case, in which a transfer coefficient is defined to be $\alpha = 0.5$, the Butler-Volmer-Equation (Eq. (5)) becomes a hyperbolic sine function and the overvoltage can be calculated according to the following equation [40]:

$$\eta_{act} = \frac{2 \cdot R \cdot T}{z_e \cdot F} \cdot \text{arsinh} \left(\frac{i}{2 \cdot i_0}\right). \tag{7}$$

Finally, the ohmic losses are determined as a function of the area specific resistance r and the operating current density i [40]:

$$\eta_{ohm} = r \cdot i. \tag{8}$$

In this study, no further losses except those mentioned above are considered, in order to simplify the calculations. Thus, the cell voltage E is determined as a difference of the Nernst-voltage and the specific losses that occur during the operation [40]:

$$E = E_N - \eta_{act} - \eta_{conc} - \eta_{ohm} \tag{9}$$

Modeling principles

The fuel cell is in general divided into several segments in the flow direction for the purpose of the simulations performed. The influence the number of segments has on the quality of the data observed will be discussed later. An illustration of a segment simulation is shown in Fig. 3a. The gas composition in the flow field of one segment is assumed to be constant and thus all the changes across the flow direction and taking the direction of the cell thickness into consideration can thus be neglected. The mass transfer only is considered for each electrode, thus enabling 1D-analysis. However, the division into several segments makes it possible to analyse the changes that occur in the flow field direction, thus enabling the 2D-analysis. The segment number is labeled with an index n. The parameter ξ describes the distance from the boundary layer electrolyte/electrode, and for the flux of species N the transport from the electrolyte layer towards the gas flow field is considered as positive. The index F always refers to the fuel electrode, whereas the index O refers to the oxygen electrode. The fuel flow velocity is indicated by v and it concerns the velocity on both the inlet and the outlet of the

segment; the velocity at the outlet is indicated by the same number n as for the corresponding segment. The index m refers to the gas component; its concentration in the fuel flow field is indicated by c, and in the electrode by a superscript b. The contacting meshes are in general considered as a part of the fuel flow field, whereas the meshes with higher layer thickness are considered as a part of the fuel electrode. In Fig. 3b the cell used is presented with the length (l) and width (b) of its electrochemically active area, as shown in Ref. [42].

As already known, in the fuel cell mode the ionic transfer occurs in the oxygen electrodes via electrolyte and further through the fuel electrode, which, because of the negative oxygen ions corresponds to the technical current direction from the fuel electrode to the oxygen electrode. Therefore, this direction is considered as positive in the fuel cell mode, and negative in the electrolysis mode. For both the fuel cell and the gas distributed along the cell, a constant temperature is assumed, and thus the thermal effects are neglected. Furthermore, in order to simplify the calculations and considering the available literature, electrochemical reactions are assumed to occur only on the boundary layer electrolyte/electrode, thus neglecting reactions in the direction of the electrode thickness. In Ref. [43], the numerical investigations carried out showed that reactions strongly diminish with increasing distance from the boundary layer electrode/electrolyte and thus the reactions can be considered to occur mainly in a region of several μm.

In the present study, considering the experimental setup and the ceramic cell housing, although a glass sealing is used, the occurrence of leakages is presumed, which lead to the water vapor production even under OCV conditions. This is considered in the model by properly corrected gas inlet composition. In addition, it is assumed that the internal leakage current occurs due to undesired gas and electrons exchange, which is considered to be constant and thus results in an offset of the polarization curve [41,44,45]. All the relevant parameters used for the purpose of the simulations are given in Table 2.

Charge transfer

The ohmic losses, ascribed to a resistance resulting from the following: (i) electron conduction in the metallic phase of the electrodes and in contacting meshes, (ii) ionic conduction in the electrolyte, as well as (iii) contact resistance between (a) single wires within the contacting meshes, (b) meshes and electrodes, and (c) individual layers; are summarized into an area specific resistance, which is thus presented as a function of the experimental setup and not solely the rSOC microstructure. Resistance of this kind is temperature-dependent and its function is displayed in the form of an Arrhenius approach [40]:

$$r = r_0 \cdot e^{-\frac{E_{a,o}}{R \cdot T}} \tag{10}$$

with a pre-exponential factor r_0 and the activation energy $E_{a,o}$. The parameter values are determined by fitting of the measured data and as such are presented in Table 2. It is assumed that this resistance is equal to the high-frequency resistance in impedance spectra.

Mass transfer in electrodes

A Dusty gas model (DGM) was used to describe the mass transfer within the porous electrodes, for which the molar flux of species N_m, the concentrations of individual gas components c_m^b and the pressure p^b are considered as a function of the coordinate ξ. If the mass transfer occurring in parallel to the cell surface is neglected, the following equation is valid for each component m [50]:

$$\sum_{\substack{l \\ l \neq m}} \frac{c_l^b \cdot N_m - c_m^b \cdot N_l}{c^b \cdot D_{ml}^e} + \frac{N_m}{D_{mK}^e} = -\frac{\partial c_m^b}{\partial \xi} - \frac{B_g \cdot c_m^b}{\mu \cdot D_{mK}^e} \cdot \frac{\partial p^b}{\partial \xi} \tag{11}$$

in which, D_{ml}^e represents the binary diffusion coefficients of the components l and m, the effective Knudsen diffusion coefficient D_{mK}^e, the permeability B_g and dynamic viscosity μ of the gas mixture. The terms on the left-hand side describe the diffusion in a multi-component system according to the Stefan-Maxwell model and the interaction of the gas components with the porous structure, whereby the last term on the right-hand side refers to the advective mass transfer in the form of a Darcy equation. For the purpose of the model simplification, the diffusion coefficients are taken into consideration as constant on the boundary to the flow channels, thus resulting in linear pressure and species quantity distribution. A comparison is made for the results observed when using constant diffusion coefficients and the data implemented from the Matlab ode 45 algorithm for a current density of ±500 mA/cm² in both fuel cell and electrolysis mode. In Fig. 4, distribution of the selected parameters for a stationary case on the fuel electrode is illustrated. The parameter values used in the model are listed in Table 2, whereby the mean size of the porous structures is estimated based on the scanning electrode microscope (SEM) images. The diagrams show that the results observed in the current range of interest can be considered as linear and they show very good accordance with the data obtained when using linear diffusion coefficients. The change in the effective diffusion coefficients within the electrode is very low and the assumption of constant values results in very low deviations that can be neglected. The effective diffusion coefficient of water vapor is lower than that of hydrogen, whereby in the fuel cell mode its partial pressure on the boundary layer electrode/electrolyte increases slightly and decreases slightly in the electrolysis mode, since in the first case water vapor is formed and in the latter case consumed. The pressure changes can also be effectively reproduced using the constant diffusion coefficients; these can be neglected, however, in the current range considered. Furthermore, a higher nitrogen fraction in the fuel mixtures leads to a decrease in the H_2O and H_2 diffusion coefficients, and as a consequence the concentration variation in the electrode increases for constant current density. Simultaneously, the influence of nitrogen on the pressure change is very low.

Mass transfer in the flow field

The mass transfer processes within the flow field are calculated based on conservation equations of mass, momentum, energy, charge as well as species balance. Under the assumption that pressure and temperature within the entire

Table 2 — Model parameters, cell geometry and charge transfer values.

Parameter	Value	Unit	Source
Length of the electrochemically active area l	$8.94\cdot10^{-2}$	m	
Width of the electrochemically active area b	$8.94\cdot10^{-2}$	m	
Electrochemical active surface $l\cdot b$	$8\cdot10^{-3}$	m^2	
Electrolyte thickness δ_E	$1.5\cdot10^{-5}$	m	[46]
Fuel electrode thickness δ_F	$3.5\cdot10^{-4}$	m	[46]
Oxygen electrode thickness δ_O	$3\cdot10^{-5}$	m	[46]
Fuel flow cross-section on the fuel side A_F	$1,2\cdot10^{-4}$	m^2	Estimated value
Flow field cross-section on the oxygen side A_O	$1,2\cdot10^{-4}$	m^2	Estimated value
Leakage on the fuel side $\dot{V}_{L,F}$	$5\cdot10^{-3}$	$\frac{l}{min}$	Measurement data
Leakage current i_L	1	$\frac{mA}{cm^2}$	[44]
Inductivity of the measuring cables L	$5\cdot10^{-9}$	H	Measurement data
Pre-exponential factor for ohmic resistance r_0	$5.47\cdot10^{-8}$	$\frac{\Omega}{m^2}$	fit
Activation energy $E_{a,o}$	$5.64\cdot10^{4}$	$\frac{J}{mol}$	fit
Fuel electrode			
Transfer coefficient α_F	0.75	–	[42]
Pre-exponential factor hydrogen-desorption γ_{H_2}	$1.22\cdot10^{8}$	$\frac{Pa}{\sqrt{K}}$	[42]
Activation energy desorption $E_{a,des}$	$8.812\cdot10^{4}$	$\frac{J}{mol}$	[42]
Pre-exponential factor γ_F	$2.2\cdot10^{8}$	$\frac{A}{m^2}$	fit
Activation energy $E_{a,F}$	$8.49\cdot10^{4}$	$\frac{J}{mol}$	[43]
Capacitance between fuel electrode and electrolyte C_F	25	$\frac{F}{m^2}$	fit
Oxygen electrode			
Transfer coefficient α_O	0.5	–	[47,48]
Pre-exponential factor γ_O	$8\cdot10^{9}$	$\frac{A}{m^2}$	fit
Activation energy desorption $E_{a,O}$	$1,2\cdot10^{5}$	$\frac{J}{mol}$	[47,48]
Capacitance between oxygen electrode and electrolyte C_O	10	$\frac{F}{m^2}$	[49]
Fuel electrode			
Average pore radius $r_{p,F}$	10^{-6}	m	SEM
Average particle diameter $d_{p,F}$	$3\cdot10^{-6}$	m	SEM
Tortuosity $\tau_{g,F}$	3.5	–	[42]
Porosity $\Phi_{g,F}$	0.35	–	[42]
Oxygen electrode			
Average pore radius $r_{p,O}$	$5\cdot10^{-7}$	m	SEM
Average particle diameter $d_{p,O}$	10^{-6}	m	SEM
Tortuosity $\tau_{g,O}$	3.5	–	[42]
Porosity $\Phi_{g,O}$	0.35	–	[42]

Table 3 — Initial operating conditions applied for model validation.

Parameter	Without H_2O	With H_2O
Temperature	800 °C	750 °C
Gas composition fuel electrode	15 % H_2, 85 % N_2	30 % H_2, 30 % H_2O, 40 % N_2
Volume flow fuel electrode	2 SLPM	2 SLPM
Gas composition oxygen electrode	21 % O_2, 79 % N_2	21 % O_2, 79 % N_2
Volume flow oxygen electrode	1.6 SLPM	1.6 SLPM

flow channels as well as the species concentration and velocity within the cross-section are constant, the mass transfer can be described based on 1D species balance equation. Numerical investigations carried out by other researchers showed that diffusion along the flow field direction has a very low impact on the polarization curve and impedance spectra, even under very high currents (>600 mA/cm²) [51]. Considering this, the species balance equation, under the assumption of ideal gas behavior, can be used as follows [52]:

$$\frac{\partial c_m^c}{\partial t} + \frac{\partial\left(c_m^c\cdot\upsilon\right)}{\partial y} = \frac{b}{A}\cdot\dot{s}_m \qquad (12)$$

with c_m^c as molar concentration, υ flow velocity, b electrochemically active width of the fuel cell, A as cross-section area
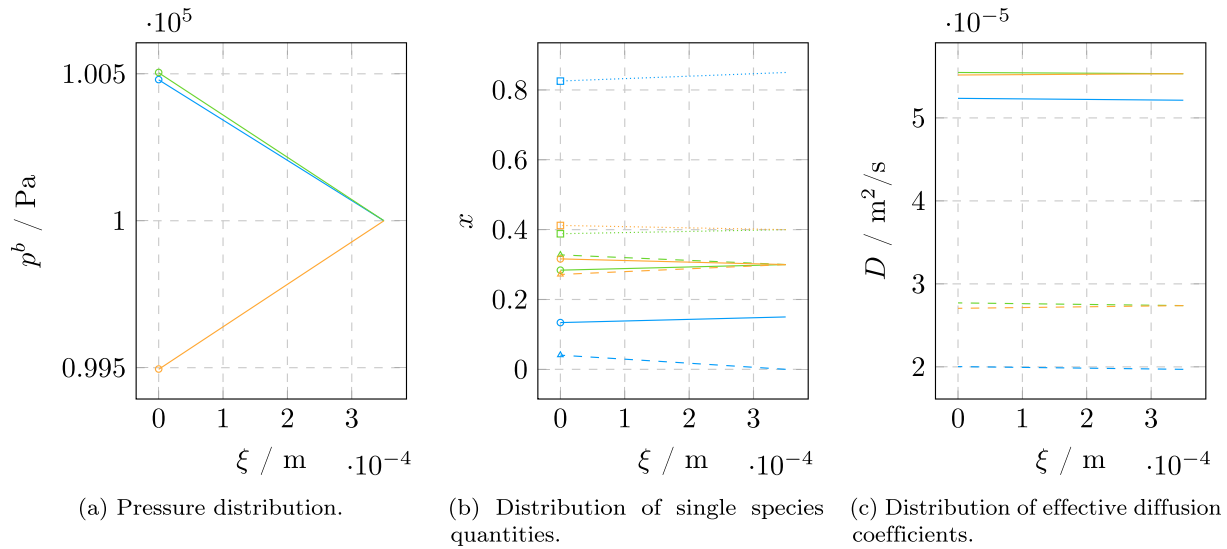
(a) Pressure distribution.

(b) Distribution of single species quantities.

(c) Distribution of effective diffusion coefficients.

Fig. 4 – **Distribution of selected parameters in the fuel electrode based on DGM (—— H_2, - - - H_2O, ········ N_2) and comparison with results using the constant diffusion coefficients ($\circ$ H_2, $\triangle H_2O$, $\square$ N_2) for species quantities in fuel flow channels for (i) —— 15 % H_2 and 85 % N_2 at 500 mA/cm², (ii) —— 30%H_2, 30%H_2O and 40%N_2 at q, and (iii) , —— 30%H_2, 30%H_2O and 40% N_2—500 mA/cm².**

of the flow channel, and $\dot{s}_m$ is the molar current density on the electrode on the boundary to the flow field. For a segment analysis a spatial discretisation of the species balance equation according to the finite difference method with the backward difference for positive flow velocity is used, as shown in the following equation [52].

$$\frac{\partial c^c_{m,n}}{\partial t} + \frac{c^c_{m,n} \bullet v_n - c^c_{m,n-1} \bullet v_{n-1}}{\Delta y} = \frac{b}{A} \bullet \dot{s}_{m,n} \qquad (13)$$

Polarization curve and impedance model
Calculation of the polarization curve occurs according to Eq. (9) (Nernst-voltage less all the occurring voltage losses, which are considered as a function of local current densities and gas composition.) The gas compositions can also be considered as a function of the operating current. In order to illustrate the cell impedance the fundamental equations are linearized and the loss potentials are approached by Taylor series. On the assumption that electrochemical reactions are characterized by a very low time constants, the frequencies examined can be considered as quasi-stationary. Therefore, there is no explicit time-dependency in the relation between potential losses that occur as a result of specific reactions. These can be calculated according to the following equation [53]:

$$\eta(i, x) \approx \eta(\bar{i}, \overline{x}) + \left.\frac{\partial \eta}{\partial i}\right|_{\_} \bullet (i - \bar{i}) + \left.\frac{\partial \eta}{\partial x}\right|_{\_} \bullet (x - \overline{x}) \qquad (14)$$

in which x depicts further current density dependent parameters. Because of the linearization applied, the system response on the harmonic input variable is the harmonic output variable with the same frequency, but the varied amplitude and the phase. Thus, the solution obtained can be presented as follows [53]:

$$i = \bar{i} + \text{Re}\left(\hat{i} \bullet e^{j \bullet \omega \bullet t}\right) \qquad \eta = \overline{\eta} + \text{Re}\left(\hat{\eta} \bullet e^{j \bullet \omega \bullet t}\right) \qquad x = \overline{x} + \text{Re}\left(\hat{x} \bullet e^{j \bullet \omega \bullet t}\right) \qquad (15)$$

Eventually, the area specific impedance z is calculated as a ratio between the voltage and current amplitudes [53]:

$$z = \frac{\hat{\eta}}{\hat{i}}. \qquad (16)$$

If the cell is considered as one segment, the entire simulation can be simplified towards 1D-simulation. It is assumed that the operating conditions remain constant within the segment and the voltage amplitude is determined as a sum of the amplitudes of single voltage losses, which are linked to the current amplitudes of the specific segment and the alternations in the gas composition due to the related transfer function. For the 2D-model, the cell is divided into several segments and in that case, it was assumed that the cell voltage and the complex amplitude are equal for all the segments. The current amplitudes give more detailed information about alternations in the gas composition in the flow channel, which impact the following segments. The overall impedance can thus be calculated according to Ref. [53]:

$$Z = \left(\sum_n \frac{b \bullet \Delta y}{z_n}\right)^{-1} \qquad (17)$$

The equivalent circuit models used to simulate impedance for both 1D- and 2D-model are shown in Fig. 5.

Model validation and experimental study

In this section the results obtained in the simulation study are presented and compared with the experimental results. Thus, model validation and an analysis of the deviations observed are provided. There are several reasons based on which differences in the simulated and measured values can occur, such as e.g. assumptions made for the model design and parameters selection. Furthermore, it is also possible that the
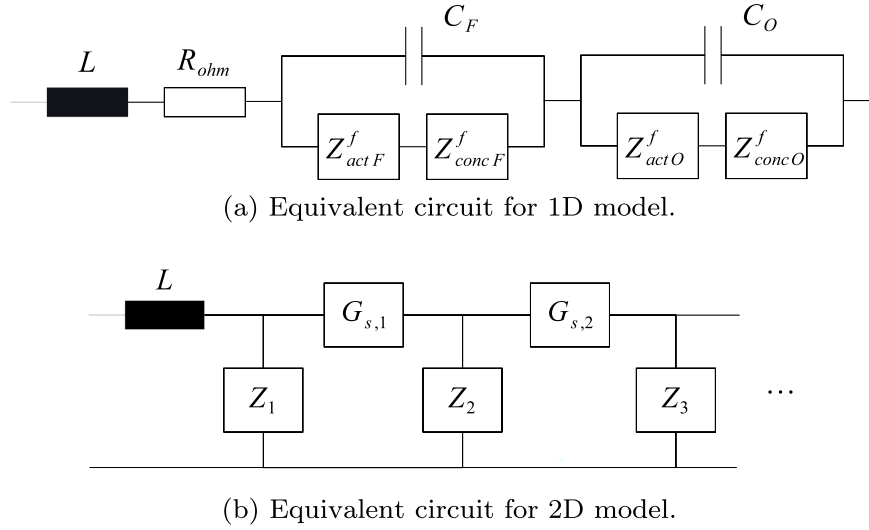
(a) Equivalent circuit for 1D model.

(b) Equivalent circuit for 2D model.

Fig. 5 – Equivalent circuit used.

experimental setup impacts the ideal operating conditions, thus causing variations of the results expected. The operating conditions under which the measured data are obtained and which are used here for the model validation can be seen in Table 3.

Detailed insights into the impact of specific parameters on the results are given here, which are the gas composition in flow channel, number of segments, flow configuration, transfer coefficient, operating temperature, fuel volume flow and fuel composition.

Gas composition in the flow channel

As already described in the previous section, the gas composition within the fuel flow field is assumed to be constant. However, there are different criteria available to determine such constant gas composition: (i) gas composition is assumed to be same on the segment inlet and outlet, (ii)

logarithmic average value of the concentration of single components at the inlet and outlet of the segments, and (iii) by cell division into 15 segments. For the purpose of simulating gas distribution in the flow field, dry hydrogen fuel was used, since it causes the highest changes of the gas composition along the cell as well as a function of operating conditions. In Fig. 6 the measured voltage (indicated by cross symbols), simulated voltage (indicated by solid black line) and single losses (represented by colored areas) are presented. When considering single losses, these are separated into activation losses (act), concentration losses caused by changes in the flow channels ($conc, chan$) and in the electrodes ($conc, diff$), on the fuel side (F), on the oxygen side (O) as well as ohmic losses (ohm).

In the first case for which the constant gas composition in the flow channel is assumed, as shown in Fig. 6a, no concentration losses occur in the flow channel, because the variation of the gas composition is not considered. Therefore,
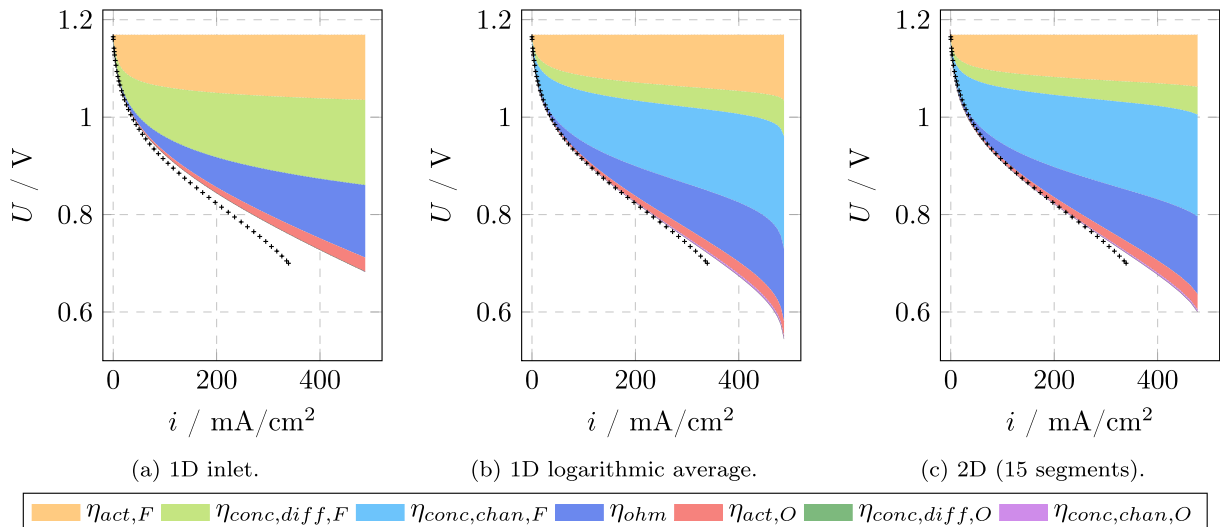

(a) 1D inlet.

(b) 1D logarithmic average.

(c) 2D (15 segments).

$\eta_{act,F}$ $\eta_{conc,diff,F}$ $\eta_{conc,chan,F}$ η_{ohm} $\eta_{act,O}$ $\eta_{conc,diff,O}$ $\eta_{conc,chan,O}$

Fig. 6 – Comparison of + the measured and — simulated polarization curves and separation of single losses as a function of different ways for determination of gas composition in the flow channels.

it is not possible to simulate losses that occur as a consequence of high operating currents and high fuel utilization rates. This is clearly visible in the diagram, since on increasing the current density, the discrepancy between the measured and the simulated curves increases significantly. In comparison, the 2D representation created by dividing the cell into 15 segments results in increasing concentration losses and slightly increasing activation losses on the fuel side with an increasing operating current, as can be seen in Fig. 6c. In the low current density range (< 100 mA/cm^2), the losses remain almost identical. The results observed using logarithmic averaging (see Fig. 6b) of the gas concentrations within the flow channels are similar to those observed for the 2D simulation. However, in this case the concentration losses first increase strongly at higher operating currents (> 400 mA/cm^2). However, in comparison to the measured data, both latter models show lower losses and with no such abrupt decrease as that observed for the measured polarization curve.

This discrepancy can on the one hand be explained as a consequence of 3D effects such as non-uniform current density distribution over the cross-sectional surface, which are not considered in this numerical study, because of the model complexity that would avoid the main goal of this study. Numerical study devoted to the investigation of fuel flow within the ceramic cell housing used [38], showed that when using the proposed geometry an area with a 25% higher flow density on the oxygen side and 15% higher on the fuel side is formed, whereby the volume flow decreases in the remaining cross-section. This could be considered through the further model extension towards a 3D model and simulation of segments in the cross-sectional direction. This was not done, however, in the present study. On the other hand, it is possible that the limited gas distribution within the flow channels causes a concentration gradient in the cross-sectional flow field, which thus leads to the greater change of the gas composition on the boundary electrode/flow channel and to increasing losses. A further reason for the changes observed could also be explained based on the results observed in Refs. [38], where it was shown that local water vapor pressure can even vary by as much as about 10%. The model accuracy could thus be increased using the computational fluid dynamic simulation tools, which simultaneously have a significant increase on the complexity of the model. Nevertheless, further explanation is not the issue in the modeling, but in the experimental setup, which is based on the leakage and not ideal contacting of the electrodes, lowering the measured cell performance.

Impact of the segment numbers on the simulation results

For a 2D perspective the cell is divided into segments and electrochemical reactions are taken into consideration for each segment. Thus, the gas composition on one segment corresponds to the gas composition obtained at the outlet of the previous segment. In this context current density is considered to be constant along each segment. On increasing the number of segments the length of each segment and the alteration within the segment decreases, while the accuracy of the simulated data increases. The impact of the number of segments on the average current density, distribution of voltage losses as well as electrochemical impedance spectra and distribution of relaxation times, for an operating voltage of 0.75 V and under operating conditions defined in Table 3, is presented in Fig. 7.

In Fig. 7a, a hyperbolic trend of the average current density as a function of segment numbers is observable, whereby the curves become flatter with the increasing number of segments. Increasing the number of segments results in a distinct increase of concentration losses in the flow field channels on the fuel side, but only in a slight increase on the oxygen side. This behavior is most pronounced until segment 5, subsequently the changes are very slight until segment 15, after which no changes are observable, as can be seen in Figs. 7a–b. When analyzing impedance data observed as Nyquist diagrams (Fig. 7c) and DRT-data (Fig. 7d), it can be seen that increasing the number of segments up to 2 results in distinct changes, for which low-frequency processes are observable. The height of the low-frequency arc increases with an increasing number of segments, but only up to the segment number 10. If the number of segments is higher than 10, no further changes occur. In the DRT spectra it is visible that even middle-frequency peaks initially increase with the increasing number of segments, and additional peaks are observed between the low- and middle-frequency peaks. Their time constant decreases with the increasing number of segments and finally they start to merge with the middle-frequency peak. The occurrence of such an additional peak may be explained by processes that occur under very low water vapor partial pressure, as at the fuel electrode inlet, and their impact decreases as the length of the segment decreases.

Impact of the flow configuration

When dividing the cell into segments, it is also possible to investigate the impact of the flow direction on the cell performance. There are in general, three different possible flow directions: co-flow, counter-flow and cross-flow. It is also possible to investigate each of these with the experimental setup used in the experimental study. Under co-flow conditions, the fuel and air directions are same, but these are in the opposite directions in the case of counter-flow. In Fig. 8 the impact of flow direction on the cell performance can be seen thus taking the voltage (Fig. 8a), current density (Fig. 8b) and species distribution (Fig. 8c) observed in the numerical study into consideration.

The polarization curves in Fig. 8a show that the impact of the flow configuration is very low under specific operating conditions. Moreover, when taking into account current distribution, it can be seen that the impact of flow configuration is low under low current densities and becomes evident only at higher operating currents. In such a case the counter-flow results in a more uniform distribution than the co-flow configuration, the reason for this is the distribution of gaseous species, as presented in Fig. 8c. On the fuel electrode side the electrochemical reactions in the fuel cell mode lead to a decrease in the hydrogen partial pressure and a water vapor increase in the flow direction, with the result that the local Nernst-voltages decrease and the concentration losses increase. The decreasing oxygen partial pressure on the oxygen
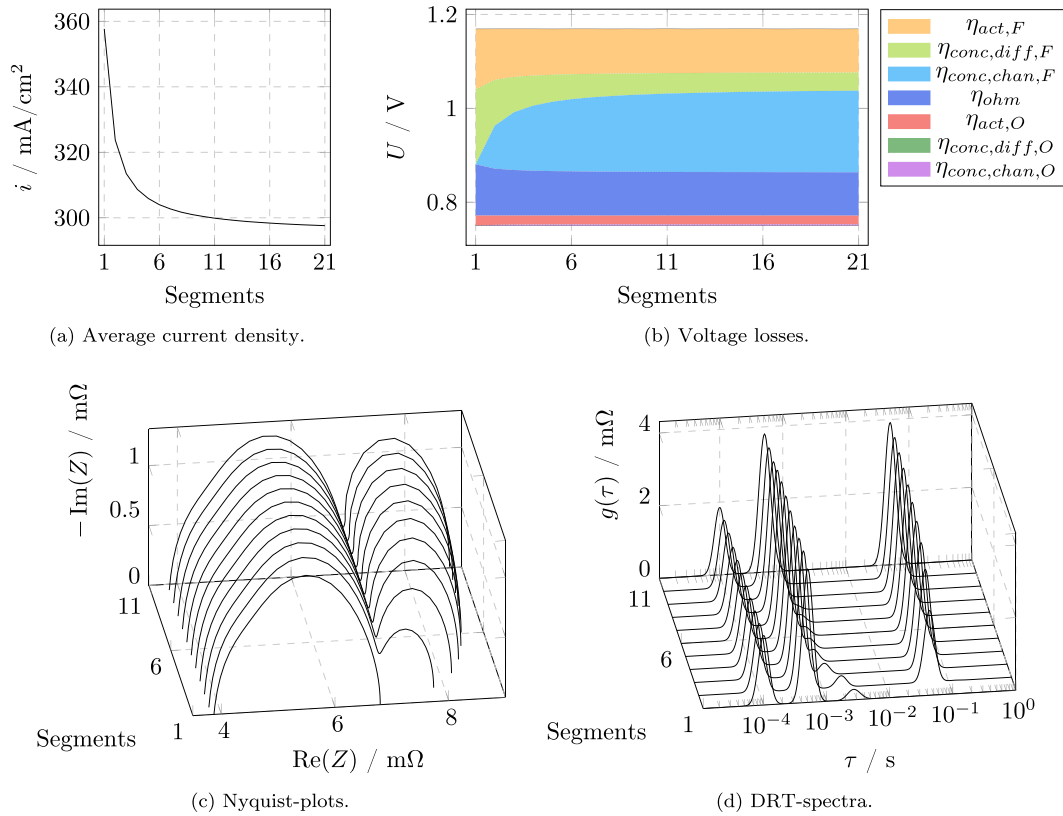
(a) Average current density.

(b) Voltage losses.

(c) Nyquist-plots.

(d) DRT-spectra.

Fig. 7 − **Impact of number of segments on the cell performance, when fueling it with dry hydrogen at 0.75 V.**

electrode causes an increase in concentration losses. Thus, under co-flow conditions the losses on both electrodes increase in the flow direction and cause a drop in the operating current. The direction of the concentration losses for the counter-flow configuration is opposite for the two electrodes, thus resulting in a more uniform current density distribution. In electrolysis mode this effect is very weak, since oxygen is formed and thus the changes in the oxygen partial pressure are lower. Moreover, the increase in the oxygen concentration increases the exchange current density on the oxygen electrode and causes lower activation losses.

In the experimental investigations performed, the fuel flow direction remained unchanged, while the air flow direction was changed in order to achieve the counter-flow configuration. The measured impedance spectra (Fig. 8d) and the corresponding DRT spectra (8e) show almost no deviations between the co-flow and counter-flow. The only difference is observed in the low-frequency range due to noise. This can be caused by changes in the temperature distribution when reversing the flow direction and also from the occurrence of leakage caused by changes in pressure distribution.

Transfer coefficient

The transfer coefficient α is a kinetic parameter, which describes the behavior of the activation energy required and thus the reaction rates of the forward and reverse reactions considered as a function of the varying electrochemical reactions and their potential within the cell [41]. In order to simulate the cell performance in a correct way, it is important

to first estimate its correct values. For simulation of fuel cells, α is usually selected to be 0.5 [29]. When simulating reversible operation, however, it is important to consider the impact of the transfer coefficient appropriate for simulating losses in both operating modes. Fig. 9a shows the activation overvoltage trend as a function of three different transfer coefficients, 0.5, 0.75 and 0.85, employing the operating conditions shown in Table 3. If $\alpha = 0.5$ (indicated by orange line) a point-symmetric behavior is observable and losses are identical in both operating modes. In the range of low current densities, a linear behavior is observable independent on the α value, thus concluding that in such a range the transfer coefficient does not impact the curve behavior. In the case if $\alpha > 0.5$, the activation losses are significantly lower for positive operating currents, based on which an asymmetric behavior is observable. An asymmetric behavior of this kind is intensified with the increasing values of transfer coefficients. Their impact is much more pronounced for negative operating currents in electrolysis mode.

The experimental investigations performed on fuel electrode-supported cells resulted in significantly higher losses when operating the cell in the electrolysis mode in comparison to the fuel cell mode. Therefore, we assume that such behavior can be linked to the asymmetric activation losses on the fuel electrode, based on which α is assumed to be greater than 0.5. In our study, since the cell is operated in a reversible mode, we performed simulations for two different α values, and compared the results obtained when employing $\alpha = 0.75$, as available in the literature [42] with $\alpha = 0.85$.

(a) Polarization curves (co-flow ——— counter-flow - - -).

(b) Current density distribution (co-flow ———, counter-flow - - -).

(c) Species distribution for 0.7 V (co-flow ———, counter-flow - - -).

(d) ——— Co-flow, ——— Counter-flow: measured Nyquist plots.
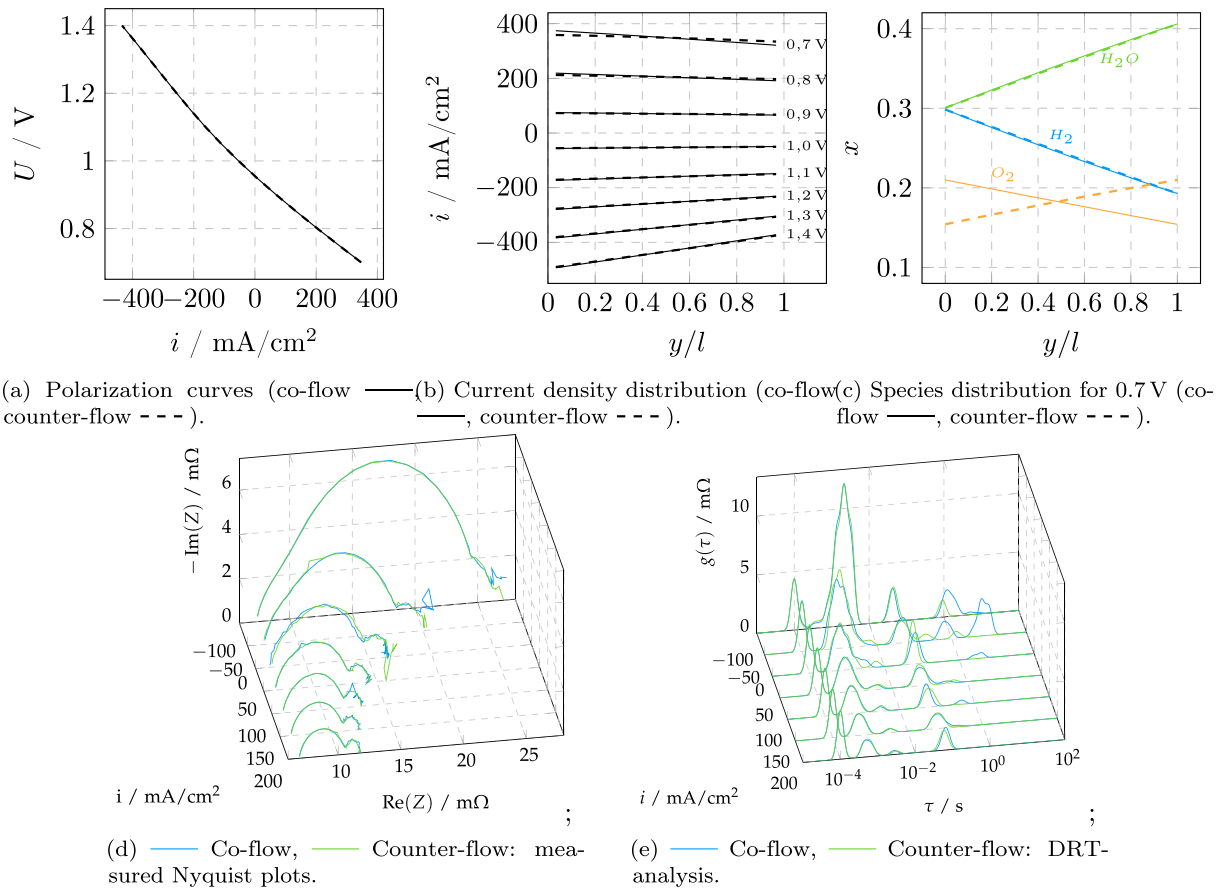
(e) ——— Co-flow, ——— Counter-flow: DRT-analysis.

Fig. 8 – Comparison of numerical and experimental results observed when fueling the cell with humidified fuel considering the co-flow and counter-flow configuration.

The results observed when employing the two different α values for the simulation study are presented and compared with the measured data in Fig. 9b for polarization curve, in Fig. 9c for EIS-spectra and in Fig. 9d for DRT-spectra. Comparison of the simulated and measured polarization curves shows that when considering the fuel cell mode, slightly lower losses are predicted for the higher α value (indicated by green solid line), whereby in the electrolysis mode significantly higher losses are predicted than for the lower α (indicated by blue solid line). The EIS- and DRT-plots provide the required explanation for such behavior, showing that this difference results mainly from the middle-frequency range and the activation losses. Under OCV conditions, the diagrams are identical for both α, since the losses in the low-current range are independent on the transfer coefficient in this case and the exchange current densities are almost the same based on the same partial pressures of H_2 and H_2O. In the DRT-spectra the middle-frequency range would appear to result in the highest deviations, which can be explained by several factors. On the one hand, the reasons are the leakage effects considered in the developed model, which cause a very low current to flow even under OCV conditions as well as the subsequent alternation of the gas composition. On the other hand, the conversion of the impedance data to the distribution of

relaxation times can result in specific artifacts. On increasing the current density, the amplitude in the middle-frequency range in the fuel cell mode decreases and increases in the electrolysis mode, the increase of which is intensified with the increasing α. Additionally, when increasing α, the dependency of the exchange current density on the water vapor concentration increases. This even intensifies the rising trend in the electrolysis mode, since the water vapor concentration decreases with increasing operating current due to the increasing quantity of hydrogen generated, thus leading to larger activation losses. In the low-frequency range the same trend is expected as for the middle-frequency range, although only apparent to a much lesser extent, which is also to be ascribed to the dependency on the exchange current density.

In comparison to the measured data, the simulation results in the entire range show lower losses, the deviation of which is higher in the electrolysis mode. The Nyquist-plots show the higher high-frequency resistance for the measured data, which can appear as a consequence of contacting issues in the experiments. The ohmic resistance values used for the simulation are obtained by curve fitting as a function of the operating temperature and based on the several measured data available. Moreover, the measured data show even stronger dependency of the middle-frequency range on the
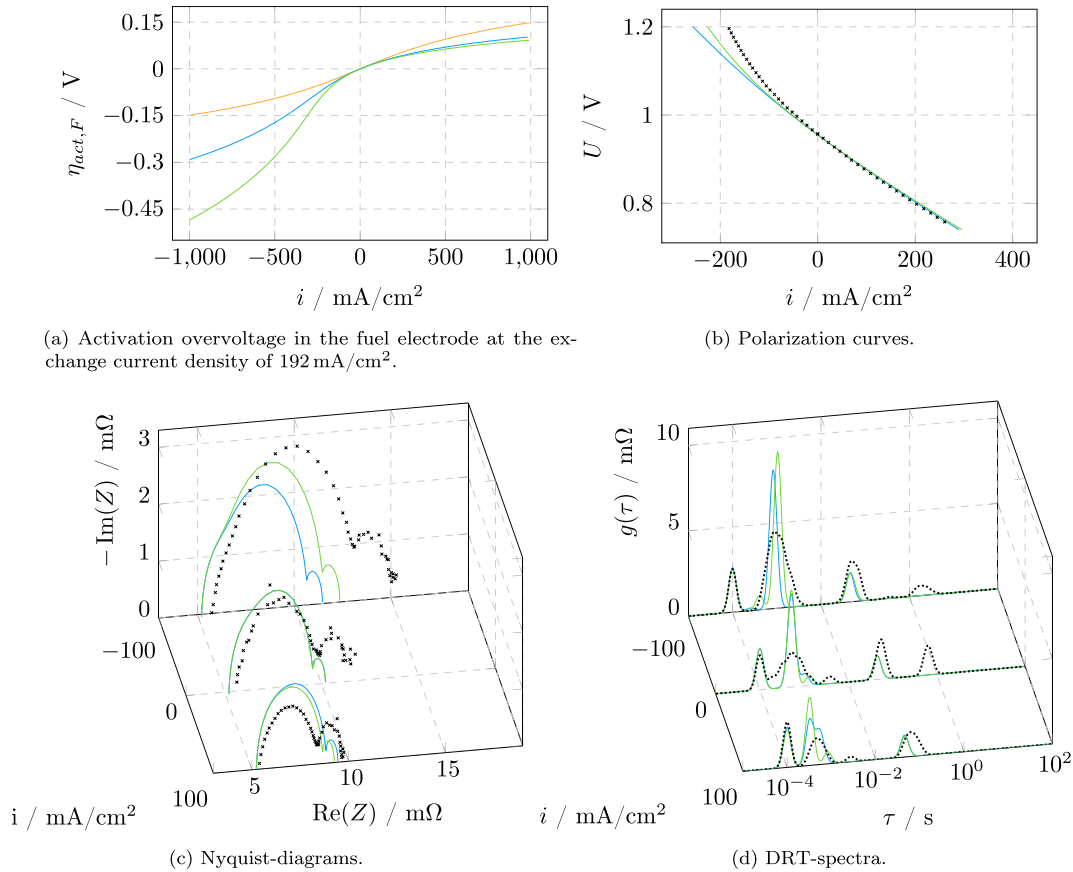
(a) Activation overvoltage in the fuel electrode at the exchange current density of $192 \, \mathrm{mA/cm^2}$.

(b) Polarization curves.

(c) Nyquist-diagrams.

(d) DRT-spectra.

Fig. 9 – **Impact of transfer coefficients of** ⎯ 0.5, ⎯ 0.75 and ⎯ 0.85 **on the cell performance and comparison with the** × **measured data.**

operating current. In this case, employing higher values for transfer coefficient results in lower deviations between the measured and the simulated data. Next, the low-frequency range of the Nyquist-plot is also lower in the simulated values, which can occur due to the processes in the flow channels, as discussed above. Such effects could also provide a specific impact in the middle-frequency range. The DRT-spectra show very good accordance of the simulated and the measured time constants. The measured data show additional peaks at approximately $\tau = 1$ s, which can be caused by the signal noise in the low-frequency range. In the simulation the time constant at $\tau = 2 \cdot 10^{-3}$ s is predicted as lower, which could refer to higher effective diffusion coefficients for the mass transfer in the fuel electrode.

Impact of operating conditions on the cell performance

In the previous sections a comparison was made between the measured and the simulated data. It could be seen that slight deviations often occur between the modeled and experimental values. The reason for this lies on the one hand in the choice of the model parameters and on the other hand on the experimental setup, in which small deviations can also result in considerable performance variations. For example, if there are leakages in the experimental setup, the volume flow can change within the flow channels and the cell. Subsequently, it causes changes of the temperature distribution and the

equilibrium state. Furthermore, depending on the fuel used, high temperature differences can occur between the cell inlet and outlet, which impact the average cell temperature, thus leading to slightly changed operating conditions in comparison to those applied in the modeling study. For this reason, the impact of three selected operating parameters: operating temperature, fuel volume flow and gas composition, on the cell performance were investigated in detail in an experimental study.

The operating temperature is an essential parameter for achieving a sufficient efficiency, both in the fuel cell and electrolysis mode, since the electrolyte conductivity increases with increasing temperature and the reaction kinetics are also enhanced. Nevertheless, the possibility for specific degradation mechanisms to occur in addition to more demanding requirements on the system components also increases simultaneously with the temperature. The impact of the operating temperature on the cell performance (T) is illustrated in Figs. 10a and b. The temperature was varied between 700 °C indicated by blue solid line, 750 °C depicted in green solid line and 800 °C illustrated by orange solid line. When varying the operating temperature, the humidified fuel mixture stated as T in Table 1 was used. It consisted of $H_2/H_2O/N_2 = 30/30/40$, with the fuel volume flow of 2 SLPM and the air volume flow of 1.6 SLPM. The measured polarization curves, as presented in Fig. 10a, show decreasing OCV with the increasing temperature. In the fuel cell mode
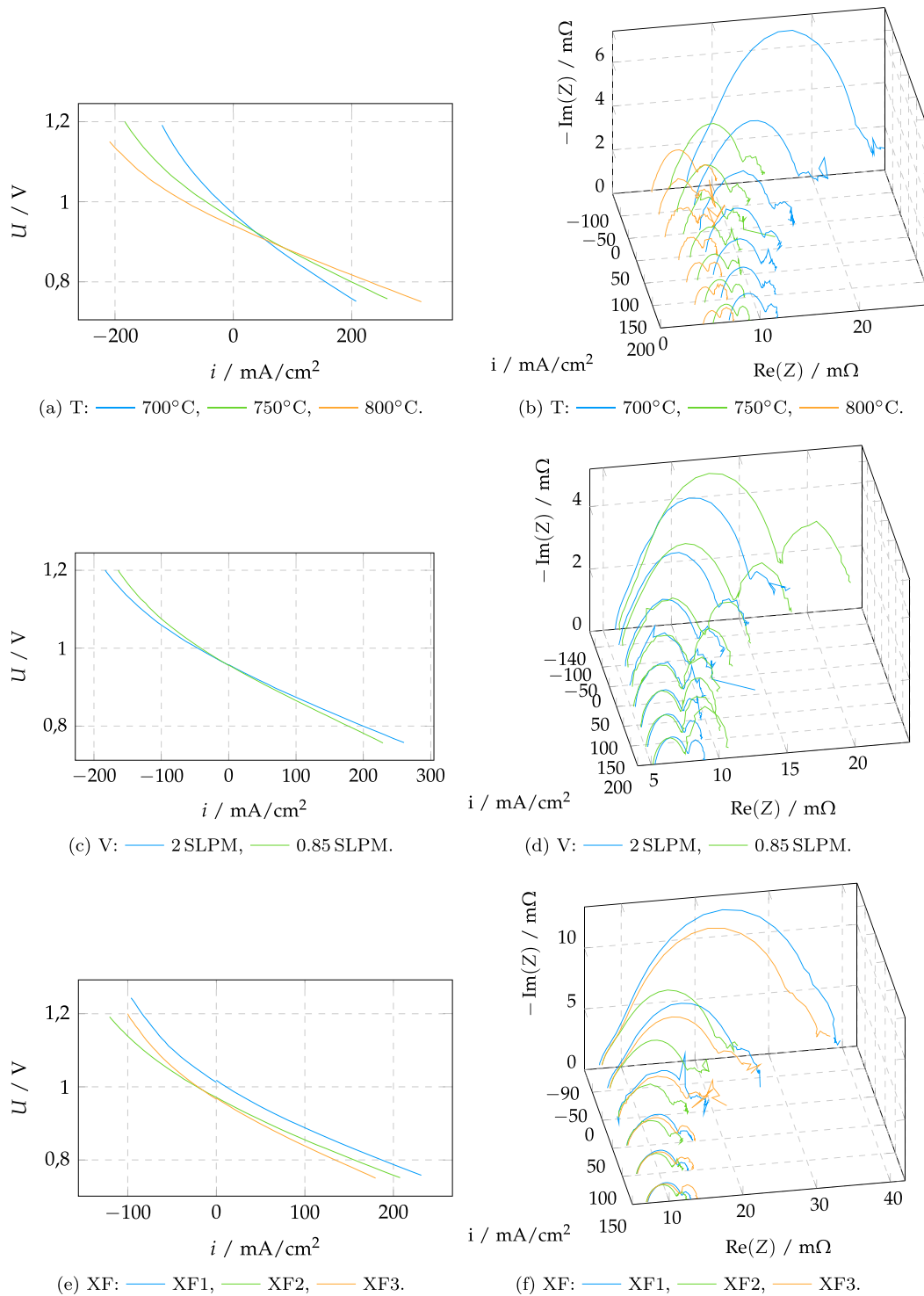
(a) T: —— 700°C, —— 750°C, —— 800°C.

(b) T: —— 700°C, —— 750°C, —— 800°C.

(c) V: —— 2 SLPM, —— 0.85 SLPM.

(d) V: —— 2 SLPM, —— 0.85 SLPM.

(e) XF: —— XF1, —— XF2, —— XF3.

(f) XF: —— XF1, —— XF2, —— XF3.

Fig. 10 − Comparison of cell performance when varying operating temperature, fuel volume flow and fuel composition.

this results in the increasing heat release, while in the electrolysis mode in the decreasing power required. Next, an increasing operating temperature reduces the polarization losses thus flattening the curve. In the fuel cell mode, an intersection point is observable and after this has been exceeded the losses are reduced. The Nyquist-plots in Fig. 10b show that while increasing the operating temperature both the ohmic resistance and high- and middle-

frequency impedance decrease. The low-frequency processes would appear to be independent of the operating temperature and the current density. Additionally, the DRT analysis was performed, which showed a peak between the low- and middle-frequency range, the amplitude of which does not vary with the varying temperature, but its time constant moves towards faster processes with the increasing temperature. This can be linked to the water vapor transport

in the fuel electrode, as observed in the simulation results referred to above.

When varying the volume flow, the velocity and thus the variation of the gas components in the fuel channel are influenced at the specific current density. The lower volume flow results in the faster variation of the chemical potential and thus increasing losses during the electrochemical reactions. Moreover, reducing the volume flow leads to an increase in fuel utilization, thus reducing quantity of unused fuel components at the fuel electrode outlet. The volume flow can also influence the temperature in the fuel cell system. The results observed when varying the fuel volume flow (V) between 2 SLPM and 0.85 SLPM are shown in Fig. 10c and d. The furnace temperature was kept constant at 750 °C, whereas on the oxygen electrode the volume flow was set to 1.6 SLPM. The fuel composition remained unchanged. By reducing the fuel flow from 2 SLPM (indicated by blue solid line) down to 0.85 SLPM (indicated by green solid line), the losses increased in the entire load range, the impact of which is even more pronounced in electrolysis mode. The impedance measurements showed no impact of the volume flow in the high-frequency range, but a significant difference occurred in the low-frequency range. This is visible for both operating modes when increasing the operating current density. In parallel, the time constant moves towards higher values thus leading to the conclusion that losses occurred that can be traced back to the mass transfer effects in the gas channels on the fuel side. In the electrolysis mode, additional losses occur in the middle-frequency range and they increase with increasing current density. This occurs on lowering the exchange current density due to the decreasing water vapor concentration, which thus causes higher activation losses.

Finally, the fuel gas composition was changed, in which the ratio between hydrogen and water vapor concentration as well as fuel dilution in nitrogen were varied. The set operating parameters can be found in Table 1, labeled as XF. The polarization curves in Fig. 10e show a clear dependence on the H_2O quantity; the higher H_2O partial pressure, the flatter the curve and lower the losses. For the OCV the H_2/H_2O-ratio is also of crucial importance according to the Nernst-equation, which is also confirmed by the measured data. The more detailed insight into losses is visible in the Nyquist-plots in Fig. 10f. Increasing the nitrogen quantity, which means

intensified fuel dilution and lower hydrogen and also the water vapor quantity, result in higher losses in the low-frequency range. If the H_2O quantity on the fuel electrode is lower, the impedance of the low- and middle-frequency range increase in the electrolysis mode with the increasing current density. In the fuel cell mode, the difference between the impedance spectra is not so pronounced. This behavior may occur as a consequence of asymmetric activation losses in the fuel electrode. Additionally, the water vapor concentration increases in the fuel cell mode due to the restricted transport in the fuel electrode and decreases in the electrolysis mode, thus amplifying the observed effect.

Relative error - simulation vs. measurement

In Fig. 11 the relative error is shown as the deviation of the simulated values in comparison to the measured values at an average current density of 100 mA/cm² in electrolysis mode and 200 mA/cm² in fuel cell mode for both transfer coefficients used (as discussed in Section Transfer coefficient). The error is illustrated for the initial operating conditions given in Table 3, as well as for the variations performed for specific parameters selected. When decreasing the water vapor quantity (down to 15 vol%) and volume flow on the fuel side (down to 0.85 SLPM) as well as increasing the operating temperature up to 800 °C, the concentration losses and their impact on the cell performance increase, which is underestimated in the simulation model leading to the higher voltages in fuel cell mode and lower voltages in electrolysis mode. With decreasing temperature the impact of activation losses increases, for which the simulation, based on its dependency on the water vapor concentration, shows lower losses in electrolysis mode and higher losses in fuel cell mode. Thus, since individual errors show the same tendency in the electrolysis mode, the total relative error increases. In contrast, in the fuel cell mode, the individual errors feature opposite tendencies, based on which the total relative error seems to be lower. The higher transfer coefficient leads on the one hand to the higher activation losses in electrolysis mode and lower losses in fuel cell mode, while on the other hand the dependency on the gas composition is intensified, thus leading to lower losses in electrolysis mode and higher losses in fuel cell mode. At a lower operating temperature of 700 °C the higher transfer coefficient results in
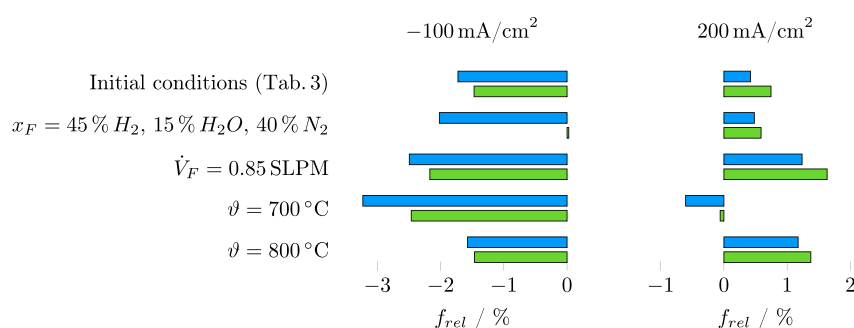
Fig. 11 – **Comparison of relative error between the simulated and measured cell voltage in both electrolysis and fuel cell mode for transfer coefficients of ▬ 0,75 and ▬ 0,85 when varying operating conditions.**

a low error in the fuel cell mode, since in this range the main deviation occurs due to the activation losses.

To sum up, the transfer coefficient of 0.85 would appear to show a lower discrepancy between the simulation and the experimental results, however, the activation losses are overestimated for low water vapor concentrations. The general trends are thus better predicted when employing a transfer coefficient of 0.75, although the losses are estimated to be lower. Nevertheless, since the gas composition as a function of the cross-sectional flow field is neglected, which influences the activation losses, the discrepancies observed are plausible. Nevertheless, for all the cases shown here, maximum relative errors of 3% in electrolysis mode and 1.5% in fuel cell mode are observed, which implies very good agreement of the simulated and measured data and confirms the suitability of the model developed to simulate processes within industrial-sized rSOCs.

Conclusion

This study gives a detailed insight into the operating behavior and loss mechanisms of industrial-sized solid oxide cells operated in a reversible mode with hydrogen/water vapor mixture. A model based on physical parameters was used for this purpose, which aids in a better understanding of the processes and behavior within the operating cell based on polarization curves, impedance data and specific losses illustrated. The model was validated with respect to varying operating temperature, volume flow and fuel gas compositions based on experiments performed in-house.

The simulated polarization curves are in a very good accordance with the measured data for both, fuel cell and electrolysis mode. The discrepancy between the measured and simulated data increased: (i) with the decreasing fuel volume flow in fuel cell mode, and (ii) with increasing operating temperature in electrolysis mode. Regarding the Nyquist, the quantitative discrepancy was observed mainly in the middle- and low frequency range, which is ascribed to the unconsidered effects occurring in the flow channels, such as non-uniform gas distribution in the flow cross-section. Next, it was identified that a non-uniform gas distribution in the flow channels has a greater influence on the voltage losses in electrolysis mode in comparison to the fuel cell mode. Taking into account varying flow configurations, the numerical and experimental studies showed no significant deviation between co-flow and counter-flow, whereby a more uniform current density distribution was achieved for the counter-flow. This could be of great importance in two cases: (i) when significantly increasing the operating currents thus increasing the heat losses, and (ii) for the case of internal reforming of hydrocarbons. Considering different approaches for determination of the gas distribution within the cell, the logarithmic averaging of the gas components between the inlet and outlet provides similar results as when dividing the cell into segments. Thus, it can be used as an alternative to reduce the computing time, especially for large systems. Focusing on the asymmetric activation losses that occur, it is not possible to fully predict performance in the electrolysis mode when performing investigations solely in fuel cell mode.

However, comparing the numerical and experimental data for different operating conditions, it is possible to link the processes that occur with the specific frequency ranges and to identify losses. In order to increase the model accuracy, further steps are possible, but the model extension toward the 3D model would be required, which would thus significantly increase the computing requirements.

In conclusion, it must be highlighted that the operating behavior of reversible solid oxide cells in industrial-size can be predicted for both operating modes in a qualitatively adequate manner. The model developed reveals the entire chemical and electrochemical analysis of the cells under investigation, enables performance prediction and eventually its optimization.

Declaration of competing interest

The authors declare that they have no known competing financial interests or personal relationships that could have appeared to influence the work reported in this paper.

Acknowledgements

Appendix. List of symbols

Symbol	Description
SOFC	Solid oxide fuel cell
Ni-YSZ	Nickel–Yttrium-stabilized-Doped zirconia
SEM	Scanning electron microscope
NO_x	Nitrogen-oxide
SO_x	Sulfur-oxide
CO_2	Carbon-dioxide
O^{2-}	Oxygen-ion
YSZ	Yttrium-stabilized-Zirconia
ϑ_{O_2}	Volume fraction of oxygen
ϑ_{N_2}	Volume fraction of nitrogen
U_{nernst}	Nernst voltage
$\Delta^r G_{T,p}$	Gibbs energy change
n^{el}	Number of electrons
F	Faraday constant
R	Universal gas constant
T	Cell operating temperature
$P_{O_{2,ca}}$	Cathodic oxygen partial pressure
$P_{O_{2,an}}$	Anodic oxygen partial pressure
i	Current density
i_0	Equilibrium exchange current density
α	Transfer coefficient
$\Delta\Phi$	Electrode over-voltage

— (continued)

Symbol	Description
$\Delta U_{Ohm}(i)$	Ohmic losses
r_A	Anode-resistance
r_E	Electrolyte-resistance
r_C	Cathode-resistance
$\Delta U_{conc}(i)$	Concentration losses
i_L	Limiting current density
D	Diffusion coefficient of reactants
c_{TPB}	Reactants concentrations on the triple-phase boundary
δ	Thickness of the diffusion layer
DGM	Dusty Gas Model
SEM	Semi-electron microscopy
μ	Dynamic viscosity
η	Overvoltage
ξ	Coordinate in electrode
δ	Layer thickness
γ	Pre-factor
Φ_g	Porosity
τ_g	Tortuosity
n	Equivalent number and number of electrons released due to fuel utilization
A	Cross-section area
N	Molar flux
y	Coordinate in flow channel
l	Length of the electrochemically active area
b	Width of the electrochemically active area
B_g	Gas permeability
p	Pressure
R	Gas constant
t	Time
i	Current density
z	Area-specific resistance
L	Inductivity
C	Area-specific capacitance
i_0	Exchange current density
i_0^0	Exchange current density under standard conditions
M	Molar mass
r_p	Pore radius
d_p	Particle diameter
$\dot{s}$	Molar flux
υ	Velocity
$\dot{V}$	Volume flow
F	Transfer function for mass transfer in electrodes
G	Transfer function for mass transfer in fuel channels
H	Transfer function for charge transfer

REFERENCES

[1] Cebulla F, Naegler T, Pohl M. Electrical energy storage in highly renewable european energy systems: capacity requirements, spatial distribution, and storage dispatch. J Energy Storage 2017;14:211–23. https://doi.org/10.1016/j.est.2017.10.004.

[2] Energy, transport and environment indicators. In: Eurostat statistical books. 2017 edition. Luxembourg: Publications Office of the European Union; 2017.

[3] Perna A, Minutillo M, Jannelli E. Designing and analyzing an electric energy storage system based on reversible solid oxide cells. Energy Convers Manag 2018;159:381–95. https://doi.org/10.1016/j.enconman.2017.12.082.

[4] Santhanam S, Heddrich MP, Riedel M, Friedrich KA. Theoretical and experimental study of reversible solid oxide cell (r-soc) systems for energy storage. Energy 2017;141:202–14. https://doi.org/10.1016/j.energy.2017.09.081.

[5] Chen K, Jiang SP. Review—materials degradation of solid oxide electrolysis cells. J Electrochem Soc 2016;163:F3070–83. https://doi.org/10.1149/2.0101611jes.

[6] Menzler NH, Sebold D, Guillon O. Post-test characterization of a solid oxide fuel cell stack operated for more than 30,000 hours: the cell. J Power Sources 2018;374:69–76. https://doi.org/10.1016/j.jpowsour.2017.11.025.

[7] Blum L, de Haart LGJ, Malzbender J, Margaritis N, Menzler NH. Anode-supported solid oxide fuel cell achieves 70 000 hours of continuous operation. Energy Technol 2016;4:939–42. https://doi.org/10.1002/ente.201600114.

[8] Fang Q, Blum L, Menzler NH, Stolten D. Solid oxide electrolyzer stack with 20,000 h of operation. ECS Transactions 2017;78:2885–93. https://doi.org/10.1149/07801.2885ecst.

[9] Frey CE, Fang Q, Sebold D, Blum L, Menzler NH. A detailed post mortem analysis of solid oxide electrolyzer cells after long-term stack operation. J Electrochem Soc 2018;165:F357–64. https://doi.org/10.1149/2.0961805jes.

[10] Trini M, Jørgensen PS, Hauch A, Bentzen JJ, Hendriksen PV, Chen M. 3D microstructural characterization of Ni/YSZ electrodes exposed to 1 Year of electrolysis testing. J Electrochem Soc 2019;166:F158–67. https://doi.org/10.1149/2.1281902jes.

[11] Jiao Z, Busso EP, Shikazono N. Influence of polarization on the morphological changes of nickel in fuel electrodes of solid oxide cells. J Electrochem Soc 2020;167:024516. https://doi.org/10.1149/1945-7111/ab6f5b.

[12] Atkinson A. Solid oxide fuel cell electrolytes—factors influencing lifetime. In: Solid oxide fuel cell lifetime and reliability. Elsevier; 2017. p. 19–35. https://doi.org/10.1016/B978-0-08-101102-7.00002-7.

[13] Martin M. Electrotransport and demixing in oxides. Solid State Ionics 2000;136–137:331–7. https://doi.org/10.1016/S0167-2738(00)00492-6.

[14] Kuznecov M. Diffusion controlled oxygen transport and stability at the perovskite/electrolyte interface. Solid State Ionics 2003;157:371–8. https://doi.org/10.1016/S0167-2738(02)00235-7.

[15] Knibbe R, Traulsen ML, Hauch A, Ebbesen SD, Mogensen M. Solid oxide electrolysis cells: degradation at high current densities. J Electrochem Soc 2010;157:B1209. https://doi.org/10.1149/1.3447752.

[16] Schefold J, Brisse A, Poepke H. Long-term steam electrolysis with electrolyte-supported solid oxide cells. Electrochim Acta 2015;179:161–8. https://doi.org/10.1016/j.electacta.2015.04.141.

[17] Chatzichristodoulou C, Chen M, Hendriksen PV, Jacobsen T, Mogensen MB. Understanding degradation of solid oxide electrolysis cells through modeling of electrochemical potential profiles. Electrochim Acta 2016;189:265–82. https://doi.org/10.1016/j.electacta.2015.12.067.

[18] Wang K, Hissel D, Péra MC, Steiner N, Marra D, Sorrentino M, Pianese C, Monteverde M, Cardone P, Saarinen J. A Review on solid oxide fuel cell models. Int J Hydrogen Energy

2011;36:7212—28. https://doi.org/10.1016/
j.ijhydene.2011.03.051.

[19] Hajimolana SA, Hussain MA, Daud WMW, Soroush M, Shamiri A. Mathematical modeling of solid oxide fuel cells: a review. Renew Sustain Energy Rev 2011;15:1893—917. https://doi.org/10.1016/j.rser.2010.12.011. http://10.1016/j.rser.2010.12.011.

[20] Bertei A, Arcolini G, Ouweltjes JP, Wuillemin Z, Piccardo P, Nicolella C. Physically-based deconvolution of impedance spectra: interpretation, fitting and validation of a numerical model for lanthanum strontium cobalt ferrite-based solid oxide fuel cells. Electrochim Acta 2016;208:129—41. https://doi.org/10.1016/j.electacta.2016.04.181. http://10.1016/j.electacta.2016.04.181.

[21] Subotić V, Schluckner C, Strasser J, Lawlor V, Mathe J, Rechberger J, Schroettner H, Hochenauer C. In-situ electrochemical characterization methods for industrial-sized planar solid oxide fuel cells part i: methodology, qualification and detection of carbon deposition. Electrochim Acta 2016;207:224—36. https://doi.org/10.1016/j.electacta.2016.05.025.

[22] Hauck M, Herrmann S, Spliethoff H. Simulation of a reversible sofc with aspen plus. Int J Hydrogen Energy 2017;42:10329—40. https://doi.org/10.1016/j.ijhydene.2017.01.189. http://www.sciencedirect.com/science/article/pii/S0360319917303579.

[23] Menon V, Fu Q, Janardhanan VM, Deutschmann O. A model-based understanding of solid-oxide electrolysis cells (soecs) for syngas production by h2o/co2 co-electrolysis. J Power Sources 2015;274:768—81. https://doi.org/10.1016/j.jpowsour.2014.09.158.

[24] Botta G, Romeo M, Fernandes A, Trabucchi S, Aravind P. Dynamic modeling of reversible solid oxide cell stack and control strategy development. Energy Convers Manag 2019;185:636—53. https://doi.org/10.1016/j.enconman.2019.01.082. http://www.sciencedirect.com/science/article/pii/S0196890419301360.

[25] Barelli L, Bidini G, Cinti G, Ottaviano A. Study of sofc-soe transition on a rsofc stack. Int J Hydrogen Energy 2017;42:26037—47. https://doi.org/10.1016/j.ijhydene.2017.08.159. http://www.sciencedirect.com/science/article/pii/S0360319917334626.

[26] Menon V, Janardhanan VM, Deutschmann O. A mathematical model to analyze solid oxide electrolyzer cells (soecs) for hydrogen production. Chem Eng Sci 2014;110:83—93. https://doi.org/10.1016/j.ces.2013.10.025.

[27] Schluckner C, Subotić V, Lawlor V, Hochenauer C. Three-dimensional numerical and experimental investigation of an industrial-sized sofc fueled by diesel reformat — part ii: detailed reforming chemistry and carbon deposition analysis. Int J Hydrogen Energy 2015;40:10943—59. https://doi.org/10.1016/j.ijhydene.2015.06.024.

[28] Yang C, Shu C, Miao H, Wang Z, Wu Y, Wang J, Zhao J, Wang F, Ye W, Yuan J. Dynamic modelling and performance analysis of reversible solid oxide fuel cell with syngas. Int J Hydrogen Energy 2019;44:6192—211. https://doi.org/10.1016/j.ijhydene.2019.01.068. http://www.sciencedirect.com/science/article/pii/S0360319919301703.

[29] Schluckner C, Subotić V, Lawlor V, Hochenauer C. Three-dimensional numerical and experimental investigation of an industrial-sized sofc fueled by diesel reformat — part i: creation of a base model for further carbon deposition modeling. Int J Hydrogen Energy 2014;39:19102—18. https://doi.org/10.1016/j.ijhydene.2014.09.108.

[30] Wang Y, Du Y, Ni M, Zhan R, Du Q, Jiao K. Three-dimensional modeling of flow field optimization for co-electrolysis solid oxide electrolysis cell. Appl Therm Eng 2020;172:114959.

https://doi.org/10.1016/j.applthermaleng.2020.114959. http://www.sciencedirect.com/science/article/pii/S1359431119362192.

[31] Peksen M, Al-Masri A, Blum L, Stolten D. 3d transient thermomechanical behaviour of a full scale sofc short stack. Int J Hydrogen Energy 2013;38:4099—107. https://doi.org/10.1016/j.ijhydene.2013.01.072. http://www.sciencedirect.com/science/article/pii/S0360319913001584.

[32] Kupecki J, Motylinski K, Jagielski S, Wierzbicki M, Brouwer J, Naumovich Y, Skrzypkiewicz M. Energy analysis of a 100kw class power to gas system based on a solid oxide electrolyzer, Energy Conversion and Management 199. 2019. p. 111934. https://doi.org/10.1016/j.enconman.2019.111934. http://www.sciencedirect.com/science/article/pii/S0196890419309252.

[33] Nechache A, Mansuy A, Petitjean M, Mougin J, Mauvy F, Boukamp BA, Cassir M, Ringuedé A. Diagnosis of a cathode-supported solid oxide electrolysis cell by electrochemical impedance spectroscopy. Electrochim Acta 2016;210:596—605. https://doi.org/10.1016/j.electacta.2016.05.014. http://10.1016/j.electacta.2016.05.014.

[34] Wan TH, Saccoccio M, Chen C, Ciucci F. Influence of the discretization methods on the distribution of relaxation times deconvolution: implementing radial basis functions with DRTtools. Electrochim Acta 2015;184:483—99. https://doi.org/10.1016/j.electacta.2015.09.097. http://10.1016/j.electacta.2015.09.097.

[35] Bao C, Bessler WG. A computationally efficient steady-state electrode-level and 1D + 1D cell-level fuel cell model. J Power Sources 2012;210:67—80. https://doi.org/10.1016/j.jpowsour.2012.03.023. http://10.1016/j.jpowsour.2012.03.023.

[36] Subotić V, Schluckner C, Joerg M, Rechberger J, Schroettner H, Hochenauer C. Anode regeneration following carbon depositions in an industrial-sized anode supported solid oxide fuel cell operating on synthetic diesel reformate. J Power Sources 2015a;295:55—66.

[37] Subotić V, Schluckner C, Hochenauer C. An experimental and numerical study of performance of large planar esc-sofcs and experimental investigation of carbon depositions. J Energy Inst 2015b;89:121—37.

[38] Schluckner C, Subotic V, Preißl S, Hochenauer C. Numerical analysis of flow configurations and electrical contact positions in sofc single cells and their impact on local effects. Int J Hydrogen Energy 2019;44:1877—95. https://doi.org/10.1016/j.ijhydene.2018.11.132. http://www.sciencedirect.com/science/article/pii/S0360319918337376.

[39] Ivers-Tiffée E, Virkar AV. Electrode polarisations. Amsterdam: Elsevier Science; 2003. p. 229—60. https://doi.org/10.1016/B978-185617387-2/50026-X. http://www.sciencedirect.com/science/article/pii/B978185617387250026X.

[40] O'Hayre R, Cha S-W, Colella W, Prinz FB. Fuel cell fundamentals. In: Fuel cell fundamentals. New Jersey: John Wiley and Sons; 2009.

[41] O'Hayre R, Cha S-W, Colella W, Prinz FB. Fuel cell fundamentals. John Wiley & Sons, Inc; 2016. https://doi.org/10.1002/9781119191766. http://10.1002/9781119191766.

[42] Zhu H, Kee RJ, Janardhanan VM, Deutschmann O, Goodwin DG. Modeling elementary heterogeneous chemistry and electrochemistry in solid-oxide fuel cells. J Electrochem Soc 2005;152:A2427. https://doi.org/10.1149/1.2116607. http://jes.ecsdl.org/cgi/doi/10.1149/1.2116607.

[43] Miyawaki K, Kishimoto M, Iwai H, Saito M, Yoshida H. Comprehensive understanding of the active thickness in solid oxide fuel cell anodes using experimental, numerical and semi-analytical approach. J Power Sources 2014;267:503—14. https://doi.org/10.1016/

j.jpowsour.2014.05.112. http://10.1016/j.jpowsour.2014.05.112.

[44] Rasmussen JFB, Hendriksen PV, Hagen A. Study of internal and external leaks in tests of anode-supported sofcs. Fuel Cell 2008;8:385–93. https://doi.org/10.1002/fuce.200800019. https://onlinelibrary.wiley.com/doi/abs/10.1002/fuce.200800019.

[45] Mogensen M, Hendriksen PV. Testing of electrodes, cells and short stacks. Amsterdam: Elsevier Science; 2003. p. 261–89. https://doi.org/10.1016/B978-185617387-2/50027-1. http://www.sciencedirect.com/science/article/pii/B9781856173872500271.

[46] Subotic V, Schluckner C, Stöckl B, Lawlor V, Schroettner H, Hochenauer C. Strategy for carbon gasification from porous ni-ysz anodes of industrial-sized asc-sofcs and effects of carbon growth. J Electrochem Soc 2016;163:F1515–22. https://doi.org/10.1149/2.0521614jes. http://jes.ecsdl.org/content/163/14/F1515.abstract.

[47] Ni M, Leung MKH, Leung DYC. Parametric study of solid oxide steam electrolyzer for hydrogen production. Int J Hydrogen Energy 2007a;32:2305–13. https://doi.org/10.1016/j.ijhydene.2007.03.001.

[48] Ni M, Leung MK, Leung DY. Parametric study of solid oxide fuel cell performance. Energy Convers Manag 2007b;48:1525–35. https://doi.org/10.1016/j.enconman.2006.11.016.

[49] Yurkiv V. Reformate-operated SOFC anode performance and degradation considering solid carbon formation: a modeling and simulation study. Electrochim Acta 2014;143:114–28. https://doi.org/10.1016/j.electacta.2014.07.136. http://10.1016/j.electacta.2014.07.136.

[50] Krishna R, Wesselingh J. The maxwell-stefan approach to mass transfer. Chem Eng Sci 1996;22:861–911.

[51] Bessler WG, Gewies S. Gas concentration impedance of solid oxide fuel cell anodes: II. Channel geometry. J Electrochem Soc 2007;154:B548. https://doi.org/10.1149/1.2720639. http://jes.ecsdl.org/cgi/doi/10.1149/1.2720639.

[52] Bao C, Bessler WG. A computationally efficient steady-state electrode-level and 1d+1d cell-level fuel cell model. J Power Sources 2012;210:67–80. https://doi.org/10.1016/j.jpowsour.2012.03.023. http://www.sciencedirect.com/science/article/pii/S0378775312006222.

[53] Orazem ME, Tribollet B. Electrochemical impedance spectroscopy. Wiley-Blackwell; 2017. https://doi.org/10.1002/9781119363682. https://onlinelibrary.wiley.com/doi/abs/10.1002/9781119363682.